Draft version
Typeset using LaTeX **twocolumn** style in AASTeX7

The Fate of Transonic Shocks around Black Holes and their Future Astrophysical Implications

Indu K. Dihingia,[1] Akhil Uniyal,[1] and Yosuke Mizuno[1,2,3,4]

[1] Tsung-Dao Lee Institute, Shanghai Jiao Tong University, 1 Lisuo Road, Shanghai, 201210, People's Republic of China
[2] School of Physics and Astronomy, Shanghai Jiao Tong University, 800 Dongchuan Road, Shanghai, 200240, People's Republic of China
[3] Key Laboratory for Particle Physics, Astrophysics and Cosmology (MOE), Shanghai Key Laboratory for Particle Physics and Cosmology, Shanghai Jiao-Tong University,800 Dongchuan Road, Shanghai, 200240, People's Republic of China
[4] Institut für Theoretische Physik, Goethe-Universität Frankfurt, Max-von-Laue-Strasse 1, D-60438 Frankfurt am Main, Germany

ABSTRACT

Theoretical models have long predicted the existence of shocks in multi-transonic accretion flows onto a black hole, yet their fate under realistic general relativistic simulations has not been fully tested. In this study, we present results from high-resolution two-dimensional general relativistic hydrodynamic (GRHD) and general relativistic magnetohydrodynamic (GRMHD) simulations of low-angular-momentum accretion flows onto Kerr black holes, focusing on the formation of shocks in transonic accretion flow. We demonstrate that for specific combinations of energy and angular momentum, global shock solutions naturally emerge between multiple sonic points. These shocks are sustained in both corotating and counter-rotating cases, and their locations depend on specific energy, angular momentum, and the spin of the black hole which is in good agreement with analytical solutions. In magnetized flows, weak magnetic fields preserve the shock structure, whereas strong fields suppress it, enhancing turbulence and driving powerful, magnetically dominated jets/outflows. The strength and structure of the outflow also depend on a black hole spin and magnetization, with higher black hole spin parameters leading to faster jets. Shock solutions are found only in super-Alfvénic regions, where kinetic forces dominate. Our findings provide important insights into the physics of hot corona formation and jet launching in low-angular-momentum accretion systems such as Sgr A* (weak jet/outflow) and X-ray binaries.

Keywords: Accretion discs (14) — Black hole physics (159) — High Energy astrophysics (739) — X-ray binaries (1811)

1. INTRODUCTION

High-energy X-ray and gamma-ray emission from black-hole accretion systems (T. M. Belloni et al. 2011) is now understood to originate very close to the event horizon, in a hot, tenuous, advection-dominated flow often referred to as the "corona". In contrast to the cooler, optically thick Keplerian disc–whose thermal multi-color blackbody spectrum contributes prominently at lower energies (N. I. Shakura & R. A. Sunyaev 1973; M. A. Abramowicz et al. 1988)–this corona is geometrically thicker and quasi-spherical, and it upscatters soft photons into a hard, power-law tail via inverse Compton processes. Modern spectral modeling, therefore, typically invokes two components: (i) the standard, high-angular-momentum disc responsible for the thermal peak, and (ii) a lower-angular-momentum, sub-Keplerian flow that becomes transonic and forms the shock-heated corona, thereby producing the non-thermal continuum (D. Molteni et al. 1996; B. Muchotrzeb & B. Paczynski 1982; S. K. Chakrabarti 2018).

Furthermore, because any infalling matter initially moves at subsonic speeds far from the black hole, it must pass through at least one sonic transition to satisfy causality and reach relativistic infall velocities at the horizon (J. Fukue 1987; S. K. Chakrabarti 1989). In low-viscosity, inviscid models, the rapidly increasing centrifugal barrier (scaling as $1/r^3$) near the black hole stalls the flow, leading to the formation of a standing or oscillating shock. Across this shock front, the gas experiences a sudden compression and heating, creating a localized jump in density and temperature. Downstream of the shock, the flow reaccelerates and becomes

Email: ikd4638@gmail.com, ikd4638@sjtu.edu.cn

supersonic and plunges into the black hole, thus naturally giving rise to the hot, Comptonizing corona that dominates the high-energy emission and is considered one of the possibilities to form such a hot corona near the black hole.

In theoretical studies of black-hole accretion, three canonical disc solutions are often employed depending on the mass-accretion rate: the radiatively inefficient, advection-dominated accretion flow (ADAF) (R. Narayan & I.-s. Yi 1994; R. Narayan & I. Yi 1995; F. Yuan & R. Narayan 2014), the optically thick, geometrically thin "α-disc," (I. D. Novikov & K. S. Thorne 1973; N. I. Shakura & R. A. Sunyaev 1973), and the optically thick, radiation-pressure–dominated "slim disc" model (M. A. Abramowicz et al. 1988). Each of these assumes that the infalling gas retains a substantial specific angular momentum, allowing it to orbit the black hole in a flattened disc structure. However, in several astrophysical environments–most notably the Galactic Center source Sgr A* (F. Melia et al. 1992; R. Narayan et al. 1995; S. M. Ressler et al. 2018), the progenitors of long gamma-ray bursts (C. L. Fryer 1999; M. J. Rees 1988), and wind-fed high-mass X-ray binaries (D. M. Smith et al. 2002; T. M. Tauris & E. P. J. van den Heuvel 2003)–the accreting material may possess only minimal angular momentum. Such low-angular-momentum flows cannot form extended Keplerian discs and instead follow nearly radial trajectories, potentially giving rise to distinct shock structures, outflows, and non-thermal emission signatures. Although these quasi-spherical, sub-Keplerian accretion regimes have received less attention than their high-angular-momentum counterparts, understanding their dynamics is crucial for interpreting the energetics, wind production, and jet launching mechanisms in these systems.

Motivated by these considerations, recent studies have explored low angular momentum accretion through both semi-analytic treatments and fully numerical simulations(e.g., D. Molteni et al. 1994; D. Ryu et al. 1995; D. Molteni et al. 1996a,b; G. Lanzafame et al. 1998; S. Das et al. 2001; D. Proga & M. C. Begelman 2003; S. K. Chakrabarti et al. 2004; S. Das 2007; K. Giri et al. 2010; T. Okuda & D. Molteni 2012; S. Das et al. 2014; T. Okuda 2014; T. Okuda & S. Das 2015; J. Kim et al. 2017; T. Okuda et al. 2019; J. Kim et al. 2019; P. Suková et al. 2017; I. Palit et al. 2019; C. B. Singh et al. 2021; T. Okuda et al. 2022; S. K. Garain & J. Kim 2023; S. Mitra & S. Das 2024; J.-X. Huang & C. B. Singh 2025). Numerous studies have demonstrated that relativistic, low-angular-momentum flows can become multi-transonic and sustain both steady and oscillatory shock fronts in 2D general relativistic hydrodynamic (GRHD) calculations. Extending these efforts into three dimensions, early 3D GRHD simulations similarly revealed the development of pulsating and radially expanding shocks (P. Suková et al. 2017). More recent high-resolution 3D GRHD runs, however, have failed to reproduce clear, long-lived standing shocks on a global scale (H. R. Olivares et al. 2023). Despite this, localized density enhancements consistent with transient shock activity have been identified in certain regions of these simulations, even though they do not manifest as coherent, system-wide shock structures.

In the present work, we focus on the formation and stability of standing shocks within general-relativistic magnetohydrodynamic (GRMHD) flows. While the existence of multiple sonic points and shock formation in low-angular-momentum flows has been established in earlier semi-analytical studies, the behavior of such shocks under the influence of magnetic fields remains elusive. In this work, we extend this classical problem into the GRHD and GRMHD regimes by systematically exploring a wide range of plasma-β values and magnetic configurations. We identify the physical conditions, particularly in terms of Alfvénic Mach number $\mathcal{M}_a$, under which global shocks are sustained or suppressed. Our study further establishes a direct connection between shock structure and outflow properties across different black hole spins. These findings provide an alternative framework to study shock-driven jet/outflow formation in weakly magnetized black hole accretion flow.

In the next section, we describe the numerical setup, and in subsequent sections, we discuss our results investigating flow properties and radiative properties. Finally, in section 6, we display our summary and add discussions based on the our findings.

2. NUMERICAL SETUP

We investigate low-angular-momentum accretion flows in a wide range of parameters using 2D ideal GRHD/GRMHD simulations with the `BHAC` code (O. Porth et al. 2017; H. Olivares et al. 2019) in modified Kerr-Schild coordinates. Simulations use spherical polar coordinates (r, θ) with logarithmic radial spacing up to $3000\, r_g$, in units where $G = M_{\rm BH} = c = 1$. With this, all length scales and time scales are presented in terms of $r_g = GM_{\rm BH}/c^2$ and $t_g = GM_{\rm BH}/c^3$, respectively. The simulation domain is resolved with an effective resolution of 1024×512 considering two levels of static mesh refinement (SMR) (base resolution 512×256), where maximum SMR levels are employed around the equatorial plane ($\pm 45°$). Additionally, to make the comparison of the study across the different

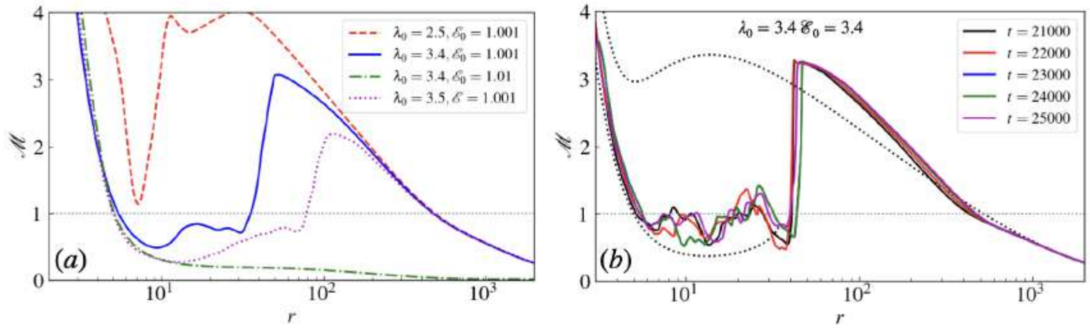

Figure 1. (a) The time and vertically averaged radial Mach number ($\mathcal{M}$) profiles for different pairs of $(\lambda_0, \mathcal{E}_0)$. (b) Vertically averaged radial Mach number ($\mathcal{M}$) profiles at different simulation times for ($\lambda_0 = 3.4, \mathcal{E}_0 = 1.001$). The horizontal dotted line corresponds to Mach number $\mathcal{M} = 1$.

black hole spins, we consider three black hole spin parameters $a_{\rm k} = -0.94, 0, +0.94$.

The initial conditions, viz., four-velocities (u^μ) and density (ρ), and pressure (p) are calculated considering $\lambda_0 = -u_\phi/u_t =$ constant, and $\mathcal{E}_0 = -hu_t =$ constant, respectively, where λ_0 and $\mathcal{E}_0$ are known as the specific angular momentum and specific energy of the fluid element. The radial four-velocity (u^r) is obtained from semi-analytical solutions for the given λ_0 and $\mathcal{E}_0$. With that, all other initial quantities can be calculated. The methods of getting the explicit expressions can be found in Appendix A. We consider the adiabatic approximation to calculate the initial gas pressure considering an index $\Gamma = 4/3$, i.e. $p = \kappa\rho^\Gamma$, where κ is a constant related to entropy. During time evolution, we use an ideal equation of state, where specific enthalpy is given by $h = 1 + \Gamma/(\Gamma-1)\ p/\rho$. In the calculation, $g_{\mu\nu}$ corresponds to the metric components of the Kerr black hole in Boyer-Lindquist coordinates.

Note that we evolve the simulations for a very long time, $t = 30\,000\,t_g$, so that the impact of initial density distribution can be minimized. During this time, our simulations reach quasi-steady states. All the time-averaged results are shown within $t = 20\,000$-$30\,000\,t_g$.

3. GLOBAL SHOCK SOLUTIONS

In this section, we want to study accretion solutions in GRHD by varying specific energy and angular momentum for the Kerr parameter $a_{\rm k} = 0.0$. For that, we choose the pairs of specific angular momentum and energy as $(\lambda_0, \mathcal{E}_0) = (2.5, 1.001), (3.4, 1.001), (3.4.1.01)$, and $(3.5, 1.001)$. The time and vertically averaged radial Mach number ($\mathcal{M} = v^r/a_s$) profiles are shown in Fig. 1 (a), where the values of $(\lambda_0, \mathcal{E}_0)$ are marked on the panel. The vertical averaging is performed within $\pm 30^\circ$ of the equatorial plane. Note that it is customary to show Mach number in the corotating frame, where the fluid reaches the black hole horizon with the speed of light. Accordingly, v^r is the radial velocity in the corotating frame and a_s is the relativistic sound speed. To show the location of sonic transitions, we show a horizontal dotted line $\mathcal{M} = 1$. The figure suggests that by choosing the specific energy and angular momentum properly, we could have accretion solutions with only the inner sonic point, only the outer sonic point, and both the critical points. The same results have also been reported before in our earlier study I. K. Dihingia et al. (2025). In addition, the figure shows that for $\lambda_0 = 3.4, 3.5$ and $\mathcal{E}_0 = 1.001$, we observe a sharp transition from supersonic to subsonic flow in between the two sonic points. Due to the time averaging, the sharp transition looks diffused. To see how the transition looks at different simulation times, in Fig. 1b, we show the vertically averaged radial Mach number profiles at different simulation times for $\lambda_0 = 3.4$ and $\mathcal{E}_0 = 1.001$. We see that during these simulation times, the transition in between is very sharp around $r \sim 40\,r_g$. Accordingly, we identify it as a shock transition, and such solutions are known as global shock solutions. Moreover, we observe that the location of the shock transition moves far from the black hole with the increase of the angular momentum.

Next, we show the time-average logarithmic normalized density ($\log_{10}(\rho/\rho_{\rm max})$) and Mach number ($\log_{10}\mathcal{M}$) distribution on the poloidal plane for the same pairs $(\lambda_0, \mathcal{E}_0)$ in the upper and lower panels of Fig. 2, respectively. The gray lines in the upper panels correspond to the velocity streamlines, and the white lines in the lower panels correspond to the sonic surface $\mathcal{M} = 1$. In the earlier study (I. K. Dihingia et al. 2025), we also reported the variation density profiles depending on the solution types. In the upper panels, we additionally observed that the origin of the outflow streamlines is close to the black hole after the shock transition (2nd and 4th columns). For solutions without shock, most of the streamlines are infalling. We find that some of the outflow emerging from close to the black hole cannot reach

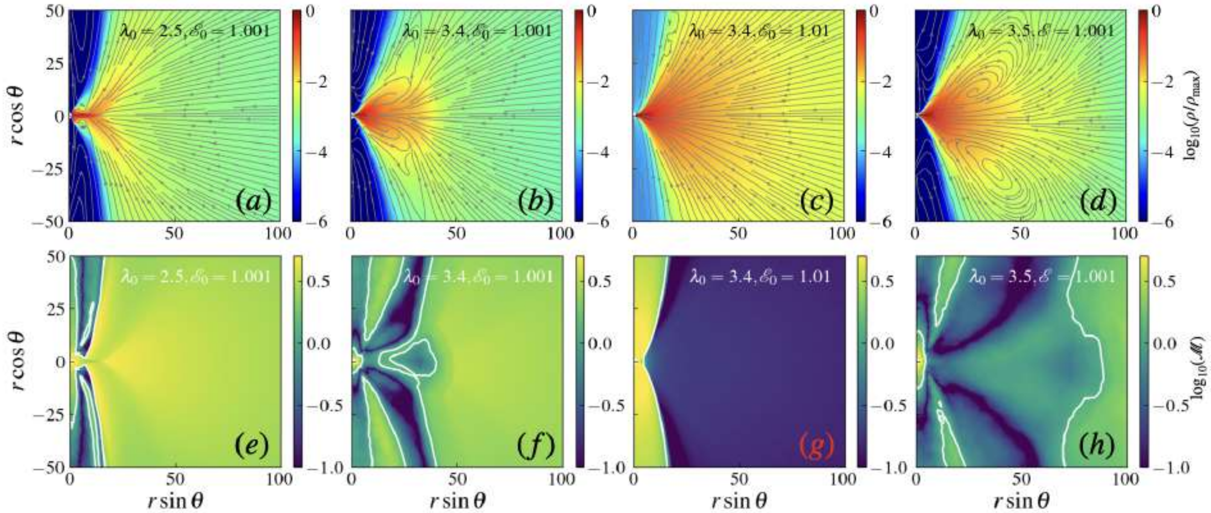

Figure 2. The time-average logarithmic (*upper panels*) normalized density ($\log_{10}(\rho/\rho_{\rm max})$) and (*lower panels*) Mach number ($\log_{10}\mathcal{M}$) distribution on the poloidal plane for different values of $(\lambda_0, \mathcal{E}_0)$. The gray lines in the upper panels correspond to the velocity streamlines, and the white lines in the lower panels correspond to the sonic surface $\mathcal{M} = 1$.

infinity. It falls back and creates vortices on both upper and lower hemisphere.

In the lower panels of Fig. 2, we observe that the Mach number is always greater than unity ($\mathcal{M} > 1$), i.e., supersonic. Depending on the values of $(\lambda_0, \mathcal{E}_0)$, we have an additional sonic surface far from the black hole (at the outer sonic surface), which we do not show here (see Fig. 9, Appendix B). In the 2nd and 4th columns, we observe the shock surface, where the flow becomes supersonic to subsonic. Additionally, for these two panels, we see supersonic outflow in the bipolar direction (see the yellowish region surrounding the rotation axis). We confirm that they are outflow, by following the velocity streamlines in the corresponding panels. In summary, we find that by choosing the $(\lambda_0, \mathcal{E}_0)$ pairs properly, we could seemingly find a global accretion shock solution.

4. VARIATION WITH KERR PARAMETERS

In the previous section, we found that by choosing $(\lambda_0, \mathcal{E}_0)$ properly, we could find global accretion shock solutions for the Kerr parameter $a_{\rm k} = 0$. In this section, we would like to extend the study for other Kerr parameters. For that in Fig. 3, we choose $a_{\rm k} = -0.94$, 0, and 0.94, and show the time-average logarithmic (*upper panels*) normalized density ($\log_{10}(\rho/\rho_{\rm max})$), (*middle panels*) Mach number ($\log_{10}\mathcal{M}$), and (*lower panels*) logarithmic Lorentz factor ($\log_{10}(\gamma-1)$) distribution on the poloidal plane for different values of chosen λ_0, while specific energy is fixed $\mathcal{E}_0 = 1.001$. In the three rows, the lines correspond to velocity streamlines, $\mathcal{M} = 1$ and $\sqrt{-g}\rho u^r = 0$, respectively. By observing the 1st and 2nd rows, we find that global accretion shock solutions exist in all the Kerr parameters. Here, we choose the angular momentum such that we have a shock solution by adjusting its values along with the value of the specific energy; the shock surface could form in different locations. In the future, one could do a parameter space survey to find the region in $(\lambda_0, \mathcal{E}_0)$ space for different Kerr parameters with global accretion shock solutions. Previous semi-analytical calculations suggest that the parameter space moves to lower angular momentum and extended energy range with the increase of Kerr parameters (H. Sponholz & D. Molteni 1994; S. K. Chakrabarti 1996a,b; I. K. Dihingia et al. 2019a).

In the third row of Fig. 3, we see that the Lorentz factor monotonically increases with the Kerr parameter. This is not similar to the well-known and well-studied Blandford-Znajek (BZ) process R. D. Blandford & R. L. Znajek (1977) , where the Lorentz factor and jet power increase with the absolute value of the Kerr parameter (S. Komissarov 2001; A. Tchekhovskoy et al. 2010, 2011; J. C. McKinney et al. 2012; A. Tchekhovskoy & J. C. McKinney 2012; M. Liska et al. 2019). In the BZ process, the jet is launched from the ergosphere; jet properties depend on its characteristics. On the contrary, for low-angular momentum flow, the jet is launched by centrifugal force and thermal pressure. For corotating cases, with the increase of the Kerr parameter, the event horizon radius becomes smaller, which leads to more gravitational compression of the flow, resulting in hotter flow as compared to a case with a lower Kerr parameter. This results in faster jet/outflow from high-spinning cases as compared to low-spinning cases. On the other hand, for the counter-rotating cases, the angular velocity ($\Omega = u^\phi/u^t$) close to the black hole is negative. However, it is a positive in the region far

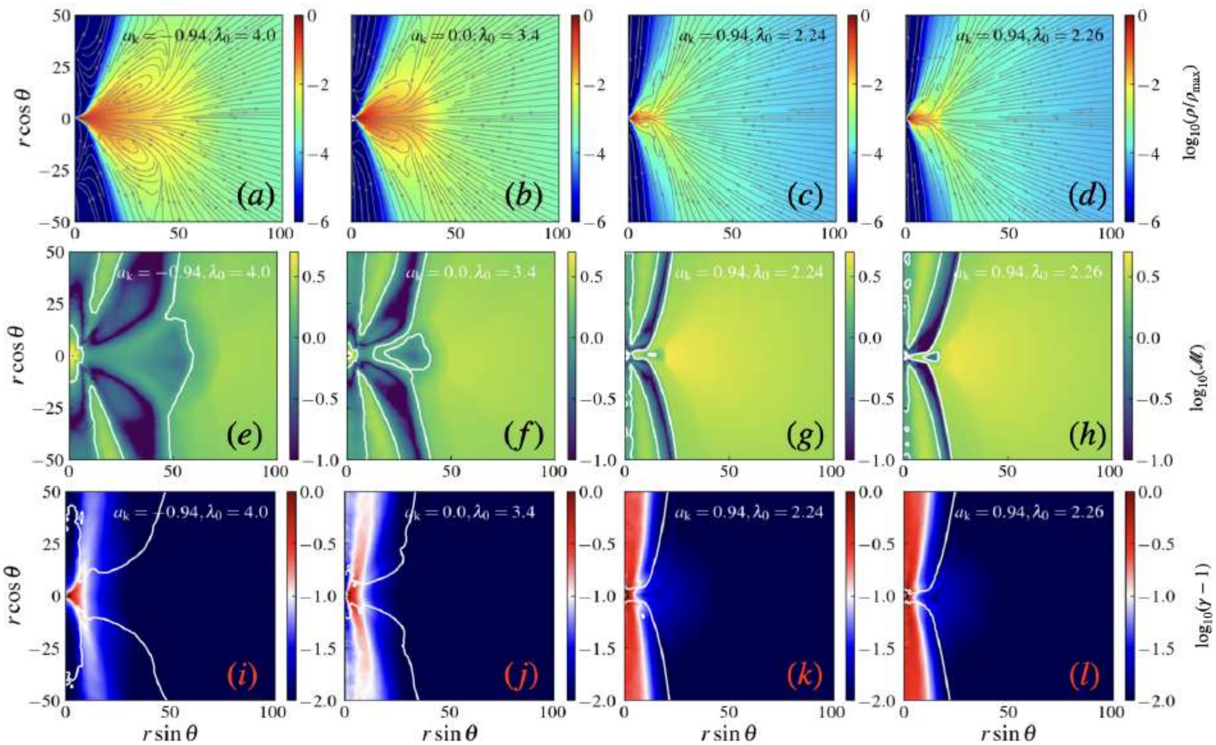

Figure 3. The time-average logarithmic (*upper panels*) normalized density ($\log_{10}(\rho/\rho_{\max})$), (*middle panels*) Mach number ($\log_{10}\mathcal{M}$), and (*lower panels*) logarithmic Lorentz factor ($\log_{10}(\gamma-1)$) distribution on the poloidal plane for different values of Kerr parameters with properly chosen ($\lambda_0, \mathcal{E}_0 = 1.001$). The gray lines in the upper panels correspond to the velocity streamlines, the white lines in the middle panels correspond to the sonic surface $\mathcal{M} = 1$, and the white lines in the lower panels correspond to the outflow surface $\sqrt{-g}\rho u^r = 0$.

from the black hole. Accordingly, the centrifugal force in the launching region depends monotonically on the Kerr parameter, resulting in a lower Lorentz factor for the counter-rotating case ($a_k = -0.94$).

5. SHOCKS IN MAGNETISED FLOW

In the previous sections, we have discussed low-angular momentum flow without any magnetic fields. In this section, we study the impacts of magnetic field strengths and configurations. In order to do that, we consider the case with $a_k = 0.94$, $\lambda_0 = 2.26$, and $\mathcal{E}_0 = 1.001$. In Fig. 4, we show the same quantities as Fig. 2 but for using different magnetic field strengths and configurations. In the first three columns, we show impacts of strengths by choosing initial plasma-$\beta_0 = 10^2$,10^4, and 10^5, considering inclined magnetic fields. In the fourth row, we show results with the initial vertical magnetic field configuration with the same initial plasma-$\beta_0 = 10^5$. We initialized the magnetic fields by supplying the vector potential as follows:

$$A_\phi(r,\theta) = \begin{cases} (r\sin\theta)^{3/4}\, \frac{m^{5/4}}{(m^2+\tan^{-2}(\theta-\pi/2))^{5/8}}\,, & \text{Inclined,} \\ r\sin\theta, & \text{Vertical.} \end{cases} \tag{1}$$

All other components of the vector potential are set to be zero. The inclined magnetic field configuration is set following C. Zanni et al. (2007); I. K. Dihingia et al. (2021). Here we use $m = 0.4$. The strength of the magnetic field is set by supplying the initial plasma-β parameter (β_0). For the current study, we chose three $\beta_0 = 10^2$, 10^4, and 10^5.

The first three columns of Fig. 4 indicate that flow structure remains similar if the magnetic field is weak enough (in this case $\beta_0 = 10^5$). In the presence of strong magnetic fields, the enhanced magnetic pressure provides additional support against gravity, effectively slowing down the radially infalling low-angular-momentum matter. This leads to a longer infall timescale, particularly in the inner regions of the accretion flow. The increased infall time allows for the growth of magnetorotational instability (MRI) (S. A. Balbus & J. F. Hawley 1991, 1998; J. F. Hawley et al. 2011, 2013). Therefore, as β_0 decreases, the flow becomes more turbulent due to a stronger magnetic field, and the flow near the equatorial plane is always subsonic except very close to the black hole. Accordingly, the density distribution becomes more extended with the increase of the magnetic field strength. In such cases, we do not observe any shock formation. For stronger magnetic field cases, we see a large portion of outflowing streamlines as compared to weak magnetic field cases, where streamlines are mostly inflow with a small portion of outflowing streamlines in the post-shock region. Additionally, we observe higher Mach numbers in the bipolar outflow region as compared to lower magnetic field cases, suggesting the development of faster and stronger outflow. This enhancement in the outflow is due to the acceleration by the magnetic pressure.

By comparing the 3rd and 4th columns of Fig. 4, we examine the effects of different magnetic field configuration: inclined versus vertical initial magnetic field. We compare them for the weak magnetic field limits. Therefore, we observe that the density distribution, velocity streamlines, and the Mach number distribution look quite similar. It suggests that the flow properties of low angular momentum accretion flow remain invariant for different magnetic field configurations, provided the strength is weak. In strong magnetic field cases, the magnetic field dominates the dynamics of the accretion flow (such as in a magnetically arrested disc, MAD). As a result, the flow properties may be drastically different.

To study the magnetized low-angular momentum accretion flow in more detail, in Fig. 5, we show the time-averaged distribution of magnetization ($\sigma = b^2/\rho$) along with poloidal field lines and the radial Alfvénic Mach number ($\mathcal{M}_a = v^r/v_a$) in the upper and lower panels, respectively, where v_a is the relativistic Alfvén velocity $v_a^2 = \sigma/(h + \sigma)$. The panels are arranged in exactly the same manner as in Fig. 4. The white solid line in the upper and lower panels shows the boundary of $\sigma = 1$ and $\mathcal{M}_a = 1$. We find that with the increase of magnetic field strength (lowering of β_0), the magnetization increases, and additionally, the region $\sigma > 1$ also monotonically increases with it. For stronger magnetic field cases, the magnetic field lines are very turbulent, whereas for weak magnetic field cases, they are organized following velocity streamlines. Suggesting kinetically/gas-dominated flow rather than magnetically dominated flow. This can be further confirmed from the Alfvénic Mach number distributions. For weaker magnetic field cases, we observe mostly super-Alfvénic ($\mathcal{M}_a > 1$) flow except in the bipolar region. This also suggests that magnetic tension and pressure play a minimal role in regulating the dynamics of the bulk flow, except near the polar axis, where magnetic field effects remain significant. On the other hand, with the increase of magnetic field strength (lowering β_0), the region $\mathcal{M}_a < 1$ increases, and overall the values of Alfvénic Mach number decrease, suggesting an increase of the magnetic control over the flow dynamics, particularly due to enhanced magnetic tension and magnetic pressure forces. Moreover, we see a global shock solution only when the flow is super Alfvénic ($\mathcal{M}_a \gg 1$). Additionally, with the vertical magnetic field case, we also see similar features, as magnetic pressure does not play a significant role in the flow dynamics for weak magnetic field limits.

Next, we would like to study the impacts of magnetic fields on jet/outflow from the accretion flow. In Fig. 6, we show the time-averaged distribution of mass flux ($\sqrt{-g}\rho u^r$), and the Lorentz factor ($\log_{10}(\gamma - 1)$ in the upper and lower panels, respectively. The solid lines in the upper and lower panels correspond to the boundary of inflow and outflow ($\sqrt{-g}\rho u^r = 0$). For weak magnetic field cases, we observe that the flow is symmetric across the equatorial plane, with bipolar outflow around the rotation axis. With the increase of the magnetic field strength, the inflow breaks its symmetry. This symmetry breaking can be attributed to the development of MRI at the inflow and outflow boundary ($\sqrt{-g}\rho u^r = 0$). We observe qualitatively similar inflow-outflow structure irrespective of the magnetic field configurations in the weak magnetic field limits. The lower panels suggest that with the increase of the magnetic field strength, the Lorentz factor of the jet increases. In very weak magnetic field cases (irrespective of the magnetic field configuration), the Lorentz factor is of the order of $\gamma \sim 2$. On the contrary, in the case of $\beta_0 = 10^2$, the value of the Lorentz factor is of the order of $\gamma \sim 10$. This is due to the activation of the BZ process for jet formation by the strong poloidal magnetic field within the ergosphere. Ideally, we could increase the magnetic field strength further; this will make the accretion flow close to the limit of the magnetically arrested disk (MAD) regime. A axisymmetric (2D) simulation, cannot capture the true nature of such MAD accretion flow. Additionally, we do not expect the flow properties of MAD achieved from traditional torus-based simulations (R. Narayan et al. 2003; A. Tchekhovskoy & J. C. McKinney 2012) or achieved by injecting a strong initial magnetic field in the low-angular momentum flow (e.g., T. M. Kwan et al. 2023; H.-S. Chan et al. 2025) to be different. They cannot be considered as truly a low-angular momentum flow (see Appendix D for more details). In such highly magnetized flow, pressure due to magnetic fields offers an additional barrier to prevent accretion flow from plunging onto the black hole, as in traditional low-angular momentum flow.

Finally, we compare time ($t = 20\,000 - 30\,000\, t_g$) and vertically averaged ($\pm 30°$) radial profiles of (a) Mach number ($\mathcal{M}$), (b) specific energy ($\mathcal{E} = -hu_t$), and (c) specific angular momentum ($\lambda = -u_\phi/u_t$) in the panels

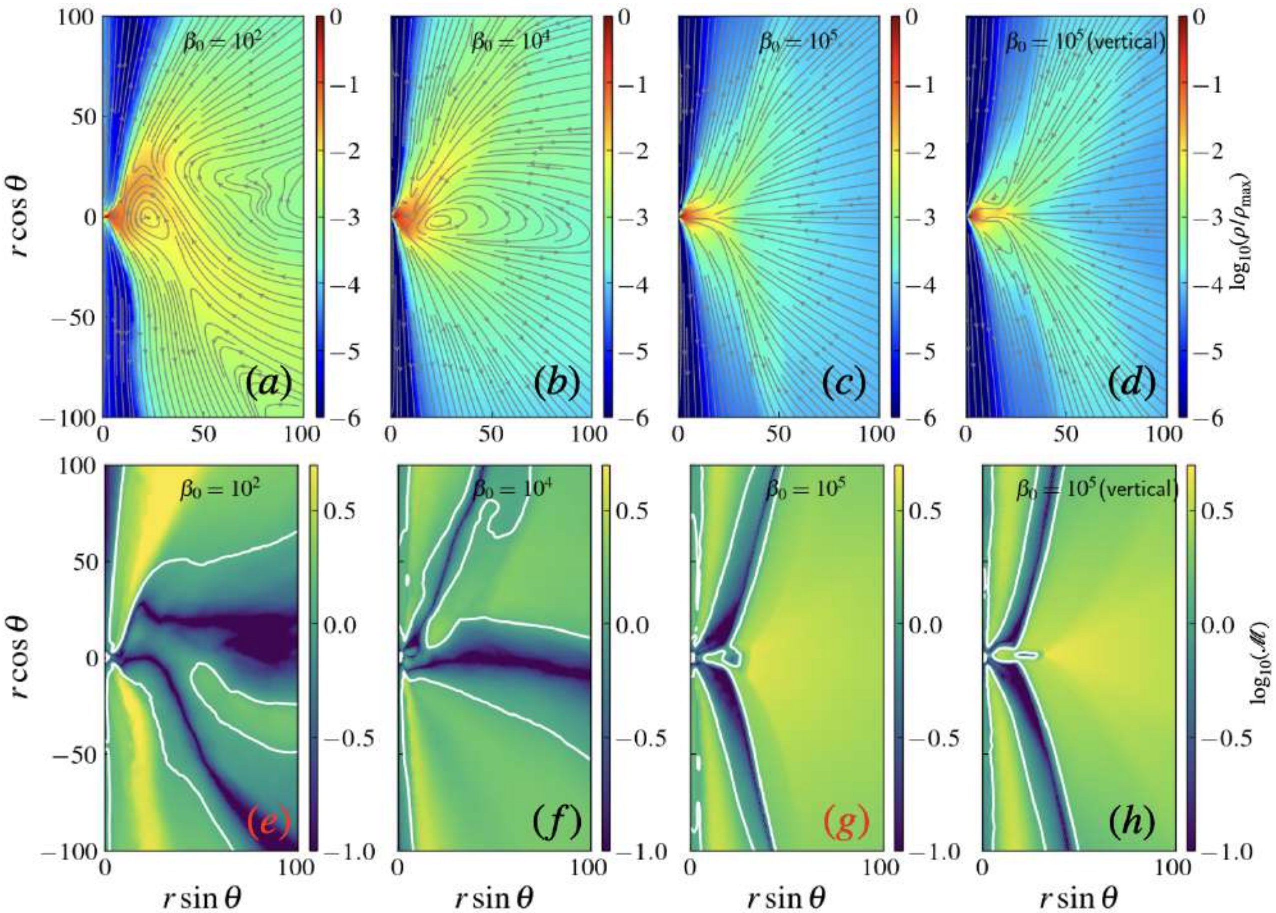

Figure 4. Same as Fig. 2 but shown in magnetized cases. From left to right column, the cases with inclined magnetic field with different plasma β_0 (10^2 (*a,e*), 10^4 (*b,f*), 10^5 (*c,g*)), and vertical magnetic field with plasma $\beta_0 = 10^5$ (*d,h*).

of Fig. 7 for different strengths of magnetic fields and configurations. As seen in the earlier 2D distributions of variables, radial profiles also suggest similar results. Even with the inclusion of a weak magnetic field (irrespective of configuration), a shock is formed. However, the shock location is slightly outside that of the hydrodynamic case due to the enhancement of the total pressure of the post-shock region by the contribution of magnetic pressure. With the increase of magnetic field strength, we observe that only the inner sonic point is available. It means that shock can not be formed under such conditions.

Panels Fig. 7b and Fig. 7c suggest that the specific energy and angular momentum are not constant to the input values $\mathcal{E}_0 = 1.001, \lambda_0 = 2.26$, which are expected to be constant if the flow is inviscid and adiabatic. The post-shock region is usually turbulent, irrespective of the magnetic field, due to inflow-outflow instability. Accordingly, we do not observe them to be conserved in the post-shock region. However, their values are conserved in the pre-shock region. Additionally, with the inclusion of magnetic fields, the accretion flow is no longer inviscid due to the presence of MRI. Accordingly, the specific energy increases due to the additional viscous heating in the flow. Similarly, the angular momentum transport increases with the increase of the magnetic field strength. As a result, we see that higher angular momentum outside and lower angular momentum close to the black hole with the increase of the magnetic field strength.

6. SUMMARY AND DISCUSSIONS

This work explores the fate of global accretion shock solutions by performing a series of GRHD and GRMHD simulations considering different Kerr parameters of the central black hole. We list the comprehensive understanding of our study below.

(1) **Existence of Global Shock Solutions:** We confirm that global accretion shock solutions form for specific values of the specific energy ($\mathcal{E}_0$) and angular momentum (λ_0), consistent with semi-analytical predictions. These shocks appear as sharp transitions between sonic points. By setting $(\lambda_0, \mathcal{E}_0)$ properly, such solutions can even be seen

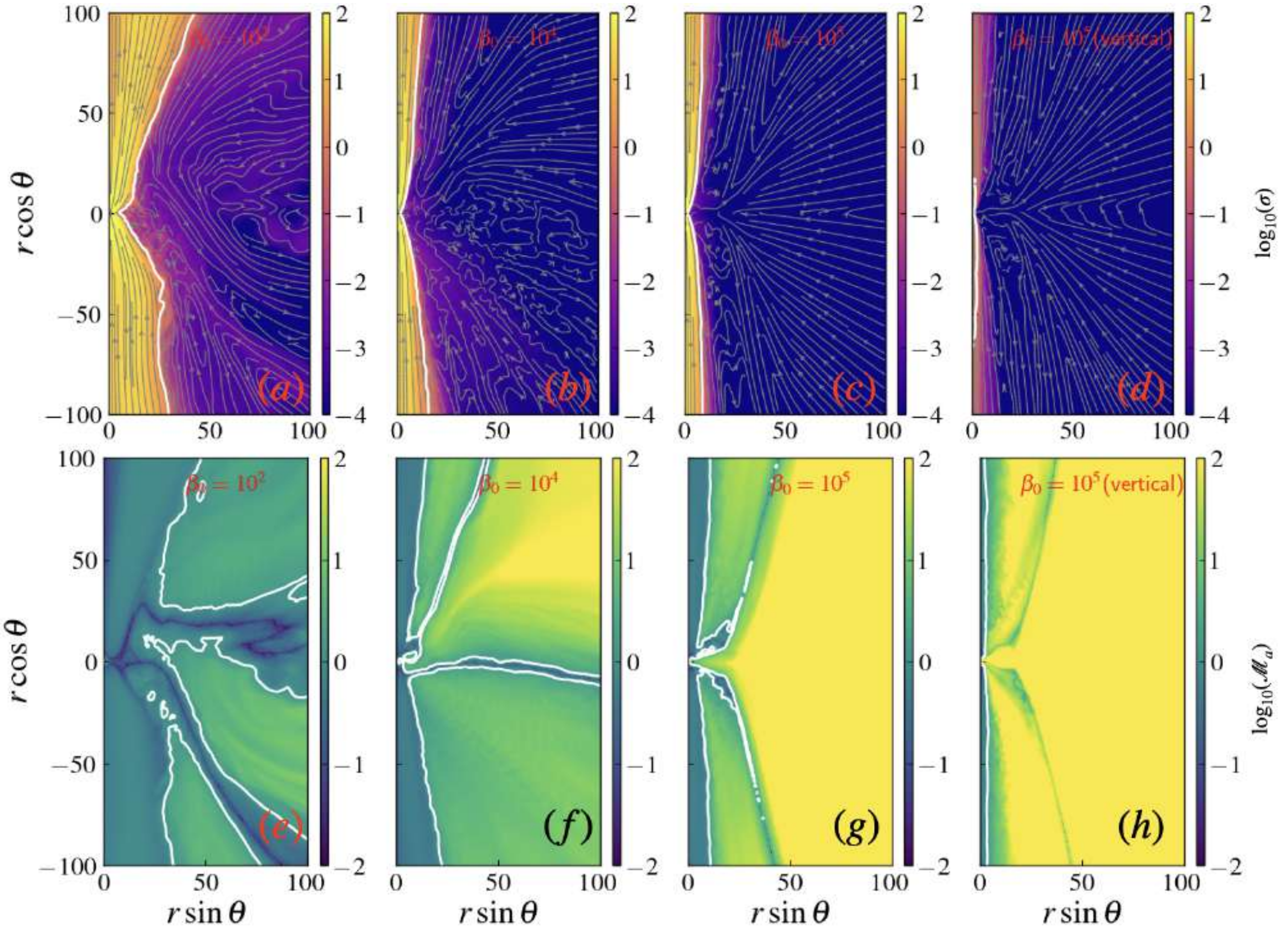

Figure 5. Same as Fig. 4 but shown time-averaged distribution of magnetization ($\sigma = b^2/\rho$ *upper*) along with poloidal field lines and the radial Alfvénic Mach number ($\mathcal{M}_a = v^r/v_a$, *lower*). The solid lines in the upper and lower panels correspond to the boundary of $\sigma = 1$ and $\mathcal{M}_a = 1$, respectively.

in all ranges of Kerr parameters, including both corotating ($a_\mathrm{k} > 0$) and counter-rotating ($a_\mathrm{k} < 0$) configurations.

(2) **Non-BZ Jet Formation:** Unlike BZ process for jet formation, jet/outflow in our models are launched primarily by centrifugal force and thermal pressure gradients. This jet formation mechanism would be able to distinguish low-angular-momentum flows from standard disc-jet systems. In this case, the jet/outflow launches from the accretion flow rather than the ergosphere of the black hole.

(3) **Jet Acceleration in Spinning Black Holes:** In the corotating case, a higher black hole spin leads to stronger gravitational compression due to the smaller size of the horizon and strong frame-dragging effect, which produces hotter post-shock flows and faster jets/outflows. The resulting outflows attain higher Lorentz factors with increasing black hole spin. In the counter-rotating case, due to the opposite nature of frame frame-dragging effect with respect to the flow, net centrifugal force decreases, resulting in the formation of weaker and slower jets/outflows.

(4) **Magnetic Field Effects on Shocks:** Very weak magnetic fields ($\beta_0 \geq 10^5$) do not significantly alter the shock structure. However, stronger fields ($\beta_0 \leq 10^2$) suppress shock formation and make the flow turbulent. Thus, the global shock solutions exist only in the limits of high super-Alfvénic flow ($\mathcal{M}_a \gg 1$). When the Alfvénic Mach number drops closer to and below unity ($\mathcal{M}_a \lesssim 1$), magnetic forces dominate, suppressing the formation of shock and changing the flow morphology by breaking equatorial plane symmetry of the accretion flow.

(5) **Jet Enhancement by Magnetization:** Magnetically dominated flows exhibit faster and more collimated jets/outflows due to strong magnetic pressure and activation of the BZ process. The

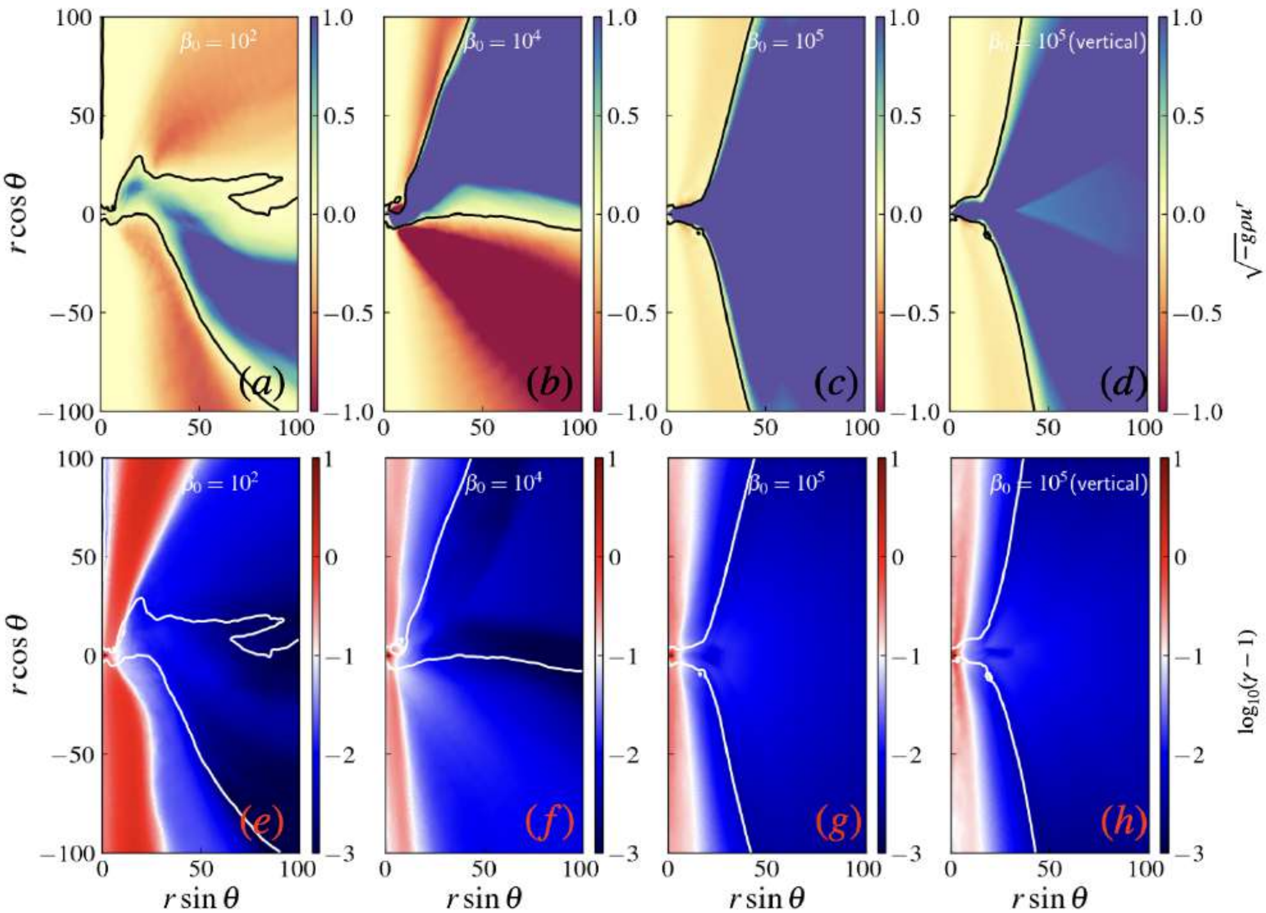

Figure 6. Same as Fig. 4 but shown the time-averaged distribution of mass flux ($\sqrt{-g}\rho u^r$, *upper*) and the Lorentz factor ($\log_{10}(\gamma - 1)$, *lower*). The solid lines in the upper and lower panels correspond to the boundary of $\sqrt{-g}\rho u^r = 0$.

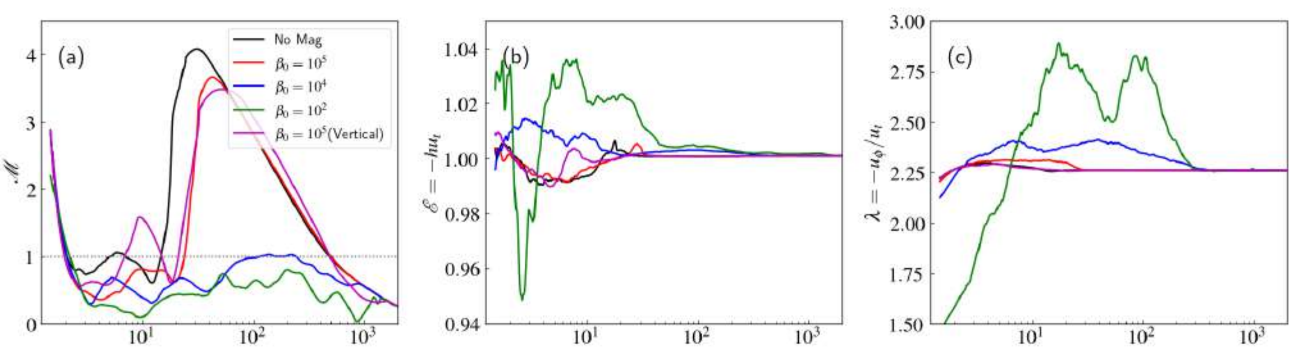

Figure 7. Radial profiles of time and vertically averaged (a) Mach number ($\mathcal{M}$), (b) specific energy ($\mathcal{E}$), and (c) specific angular momentum (λ) for different magnetic field strengths and configurations.

Lorentz factor increases from $\gamma \sim 2$ in weak fields to $\gamma \sim 10$ in strong magnetic fields.

(6) **Magnetic Configuration Robustness:** The flow structure is largely insensitive to the magnetic field geometry (inclined vs vertical) in the weak-field limit. The shock and jet properties remain qualitatively similar in both configurations. However, by increasing the magnetic field strength, we may find differences in the flow properties.

(7) **Impact on Flow Energetics and Transport:** Strong magnetic fields enhance angular momentum transport and heating via MRI. As a result,

energy and angular momentum are not conserved downstream of the shock, especially in highly magnetized regions.

Although multi-transonic accretion flows and associated shock structures arise naturally in idealized inviscid and adiabatic models, their realization in actual astrophysical environments around well-known and well-studied astrophysical sources is elusive. Realistic accretion flows are highly dynamic and turbulent, shaped by viscosity, radiative cooling, and magnetic fields, all of which can suppress or destabilize multiple sonic points. Earlier semi-analytic studies also suggest that shock parameter space reduces with viscosity and radiative cooling, and it vanishes in extreme limits (e.g., S. Das & S. K. Chakrabarti 2004; S. K. Chakrabarti & S. Das 2004; R. Kumar & I. Chattopadhyay 2013; I. Chattopadhyay & R. Kumar 2016; I. K. Dihingia et al. 2018b, 2019a, 2020; A. Kumar et al. 2025). We have also seen the same trend with magnetic field strength. Additionally, the formation of global shock solutions requires fine-tuned combinations of specific angular momentum and energy, conditions that may or may not be generically satisfied for all AGN or Black hole X-ray binaries (BH-XRB) environments. Consequently, even when transient or localized shock-like features arise, they may be short-lived or masked within a turbulent background. It suggests that the presence of long-lived, large-scale shocks is less likely in nature. Thus, these solutions are merely very good tools to understand idealized accretion flow.

Despite that, we expect such multi-transonic solutions, with shocks and without shocks, can still be useful in certain astrophysical environments, at least in weak magnetic field limits. We list some of such environments (but not all) below:

(1) **Radiative inefficient phase of BH-XRBs outburst:** Transient BH-XRBs exhibit episodic outbursts lasting from several weeks to months, during which their X-ray luminosity can increase by factors of thousands relative to quiescence. These dramatic flares are generally attributed to a sudden rise in disc viscosity at the "pile-up" radius, which triggers a rapid inward transport of mass governed by the low angular momentum system (S. K. Chakrabarti 1989, 1990; S. K. Chakrabarti 1996c; S. K. Chakrabarti et al. 2019; R. Bhowmick et al. 2021). Accordingly, the GRMHD solutions developed here may offer valuable insights into the outburst behavior of black-hole X-ray binaries, and we intend to investigate this application in future work. Future three-dimensional (3D) GRMHD simulations will be able to decipher the physics of observed X-ray polarizations of the black hole sources (e.g., N. Rodriguez Cavero et al. 2023; J. F. Steiner et al. 2024; A. Garg et al. 2024; S. Majumder et al. 2025).

(2) **Variability in Sgr A*** GRMHD models typically predict rapid, large-amplitude variability in the simulated light curves, which contrasts sharply with the relatively smooth, low-variability emission observed from Sgr A* (L. Murchikova & G. Witzel 2021; K. Akiyama et al. 2022; L. Murchikova et al. 2022; M. Wielgus et al. 2022). Observations now suggest that Sgr A* is primarily fed by the stellar winds of ~ 30 massive stars orbiting at parsec scales (E. Quataert 2004; J. Cuadra et al. 2008; S. M. Ressler et al. 2018), resulting in an essentially wind-fed, low-angular-momentum accretion flow rather than a rotation-supported disc. Consequently, extending our sub-Keplerian, low angular momentum GRMHD model for Sgr A* may help in understanding the observed variability and will form the basis of our future investigations.

Therefore, with the weak magnetization, our multi-transonic GRMHD solutions (with or without shocks) provide a unified framework for modeling low-angular-momentum accretion in a variety of astrophysical settings. Along with the above-mentioned points, our setup can also be used to understand the dynamics of tidal disruption debris, fallback accretion in supernovae and gamma-ray bursts, and low-luminosity active galactic nuclei (AGN) fed by Bondi-type spherical accretion flows. Overall, these solutions capture the interplay between shock formation, flow topology, and radiative inefficiency under weak magnetic fields, offering new insights into diverse accretion phenomena.

Finally, we would like to mention that this study is confined to axisymmetric (2D) GRHD and GRMHD simulations without performing any radiative transfer, thereby restricting the capacity to fully capture three-dimensional turbulence, which could provide direct comparison with observational signatures such as spectra, variability, or polarization. Note that our earlier study hints that radiative properties have direct dependencies on the types of low-angular momentum solutions (I. K. Dihingia et al. 2025). It is expected that the low-angular momentum flow is quasi-spherical, and therefore, we expect similar results from the 3D simulations. However, with the increase in magnetic field strengths, such simulations are indeed required. Therefore, the logical progression is to expand the current study with 3D GRMHD simulations and integrate radiative post-processing to evaluate observational significance. These efforts are presently in progress and will be communicated in due time.

ACKNOWLEDGMENTS

This research is supported by the National Key R&D Program of China (Grant No. 2023YFE0101200), the National Natural Science Foundation of China (Grant No. 12273022), the Research Fund for Excellent International PhD Students (grant No. W2442004) and the Shanghai Municipality orientation program of Basic Research for International Scientists (Grant No. 22JC1410600). I.K.D. acknowledges the TDLI postdoctoral fellowship for financial support. The simulations were performed on the TDLI-Astro cluster in Tsung-Dao Lee Institute, Pi2.0, and Siyuan Mark-I clusters in the High-Performance Computing Center at Shanghai Jiao Tong University. This work has made use of NASA's Astrophysics Data System (ADS).

DATA AVAILABILITY

The simulation data and analysis scripts used in this work are available upon reasonable request.

APPENDIX

A. INITIAL CONDITIONS

By simple steps of calculations, with the help of the GRHD equations, the radial derivatives of the radial velocity on the equatorial plane in the corotating frame can be expressed as $dv/dr = \mathcal{N}/\mathcal{D}$. For explicit expressions of the GRHD equations on the equatorial plane and $\mathcal{N}$ and $\mathcal{D}$, please follow I. K. Dihingia et al. (2018a, 2019b). We solve the equations from the sonic point, where $\mathcal{N} = \mathcal{D} = 0$ simultaneously. Depending on the input parameters, viz., specific energy $\mathcal{E}_0 = -hu_t$, and specific angular momentum $\lambda_0 = -u_\phi/u_t$, we can have either one or three sonic points. At the sonic points, we use L'Hôpital's rule to get the two values of the velocity gradient ($dv/dr|_c$). If the sign of both values of $dv/dr|_c$ is real and opposite, such points are known as saddle type or 'X-type'. If they are of the same sign, sonic points are known as nodal type. Finally, if the values are imaginary, then the sonic points are known as 'O-type'. Here, we only consider 'X-type' sonic points with a '-ve' sign for $dv/dr|_c$, which corresponds to the accretion solution. We solve dv/dr and $d\Theta/dr$ (temperature gradient: $\Theta = p/\rho$) starting from the sonic point towards both sides and joining them, we get the full accretion solution connecting the event horizon and infinity. After that, we use the solution $v(r)$ to get all the initial conditions as follows:

$$
\begin{aligned}
u^r(r,\theta) &= -g_{rr}^{1/2}\frac{v(r)}{\sqrt{1-v^2(r)}}f(r,\theta), \quad u^\theta(r,\theta) = 0,\\
u^\phi(r,\theta) &= g^{\phi\phi}u_\phi + g^{t\phi}u_t, \quad u^t(r,\theta) = g^{tt}u_t + g^{t\phi}u_\phi,\\
\rho(r,\theta) &= \left[\frac{\Gamma-1}{\kappa\Gamma}(h_0-1)\right]^{\frac{1}{\Gamma-1}}, \quad p(r,\theta) = \kappa\rho^\Gamma,
\end{aligned}
\tag{A1}
$$

where

$$
h_0(r,\theta) = \sqrt{\frac{(2\lambda_0 g^{t\phi} - g^{tt} - \lambda_0^2 g^{\phi\phi})\mathcal{E}_0^2}{1+g_{rr}(u^r)^2}}, \quad u_t(r,\theta) = -\mathcal{E}_0/h_0, \quad u_\phi(r,\theta) = -\lambda_0 u_t. \tag{A2}
$$

Here $f(r,\theta)$ is an assumed function, which models the distribution along the vertical direction. For simplicity, we consider that u^r increases in the vertical direction depending on a scale height, which is given by

$$
f(r,\theta) = \exp\left[-\left(\frac{r\cos\theta}{r\sin\theta + r_{\rm H}}\right)^2\right]. \tag{A3}
$$

The function is motivated by our earlier study with long-term evolution (I. K. Dihingia et al. (2025)). We find that the outer part of the accretion flow follows $u^r(r,\theta) = u^r(r,\pi/2)\exp(-(r\cos\theta/\alpha)^2)$. We could roughly set $\alpha = r\sin\theta + r_{\rm H}$, the plot of α and $r\sin\theta + r_{\rm H}$ is shown in Fig. 8.

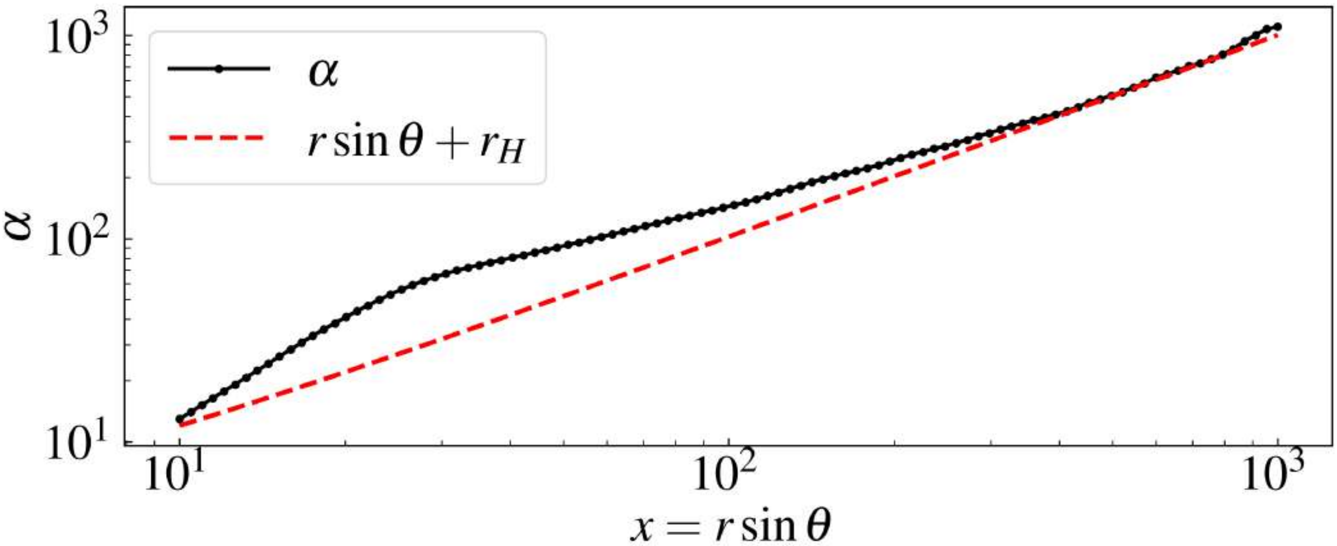

Figure 8. Variation of α along the disc radius (see Appendix A for more details).

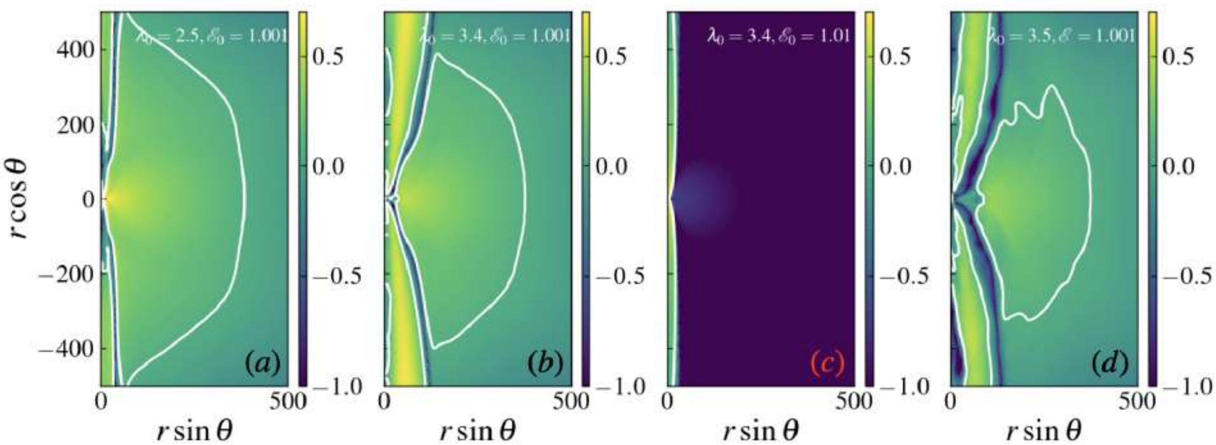

Figure 9. Same as Fig. 2 but shown larger spatial scale.

B. OUTER SONIC SURFACE

In Fig. 2 (upper panels), we show the flow properties only within $r < 100\,r_g$. However, the outer sonic points in Fig. 1 are around $r \sim 500\,r_g$. To capture the outer sonic surface, in Fig. 9, we show the distribution of Fig. 2 (upper panels) up to $r < 500\,r_g$. The panels show extended outer sonic surfaces for panels (a), (b), and (d). We observe that the outer sonic surface is missing for panel (c), indicating that the solution related to this particular choice of $(\lambda_0, \mathcal{E}_0)$ does not exhibit an outer sonic point.

C. ANGULAR VELOCITY IN DIFFERENT BLACK HOLE SPIN CASES

Earlier, we have seen that the jet Lorentz factor increases monotonically with the value (not the absolute value as in the BZ process) of the Kerr parameter. Since the jet/outflow launches from close to the black hole rather than the black hole ergosphere itself. Therefore, the Lorentz factor depends on the gravitational compression as well as the net centrifugal force, which depends on the angular velocity $\Omega = u^\phi/u^t$. In Fig. 11, we show the angular velocity close to the black hole for three different Kerr parameter cases with $\mathcal{E}_0 = 1.001$. The value of black hole spin and specific angular momentum is marked on each panel. For the highly spinning case ($a_{\rm k} = 0.94$), we observe very high angular velocity around the bipolar region, which is not the case for $a_{\rm k} = -0.94$. In counter-rotating case with $a_{\rm k} = -0.94$, the

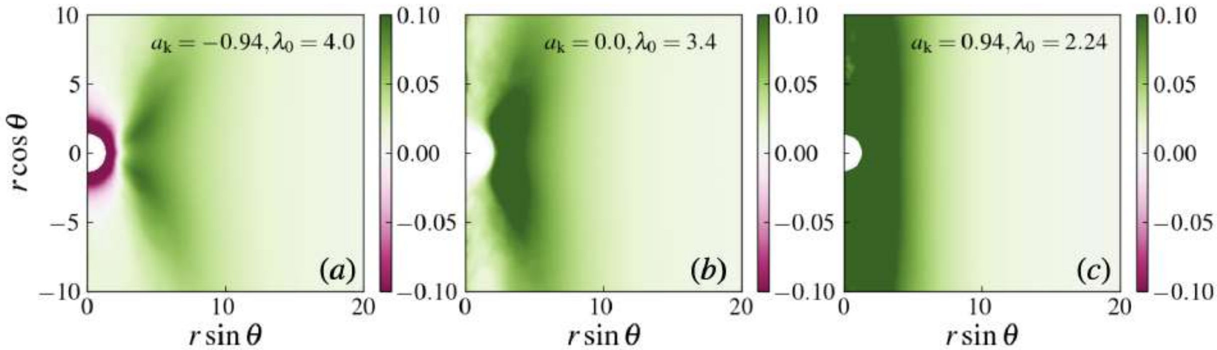

Figure 10. Distribution of angular velocity $\Omega = u^\phi/u_t$ for different simulation models with different Kerr parameters.

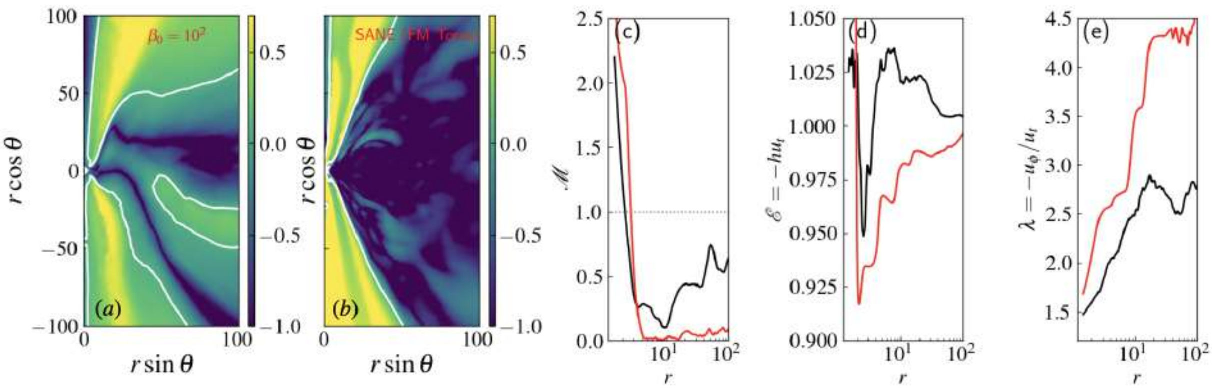

Figure 11. Time-averaged Mach number ($\mathcal{M}$) distribution for (a) low-angular momentum flow with $\mathcal{E}_0 = 1.001, \lambda_0 = 2.26, \beta_0 = 10^2$ and (b) SANE FM torus. White contours in these two panels correspond to $\mathcal{M} = 1$. Panels (c), (d), and (e) show the vertically averaged and time-averaged Mach number, specific energy, and specific angular momentum, respectively, for the FM torus (red) and low-angular momentum (black). The horizontal dotted line in panel (c) corresponds to $\mathcal{M} = 1$.

angular velocity is negative very close to the black hole, which is expected due to the frame-dragging effects. For the zero-spinning case, we observe a higher value of angular velocity than that of the counter-rotating case. The maximum angular velocity region resides off the bipolar region for $a_k = 0$ (see Fig. 9).

D. COMPARISON WITH HYDROSTATIC EQUILIBRIUM TORUS

We have seen in Sec. 5 that, with the increase in magnetic field strength, the flow becomes mostly subsonic far from the black hole. In this section, we compare it with Standard and Normal Evolution (SANE) Fishbone-Moncrief torus simulation following L. G. Fishbone & V. Moncrief (1976). We set $r_{in} = 6\,r_g$ and $r_{max} = 12\,r_g$ and evolved it up to $t = 12000\,t_g$ with a single-loop poloidal magnetic field. We perform a time-averaging with the range of $t = 10000 - 12000\,t_g$ for comparison with our earlier simulation of the case with parameters $\mathcal{E} = 1.001$, $\lambda_0 = 2.26$, $\beta_0 = 10^2$, and $a_k = 0.94$. Fig. 11 shows the time-averaged Mach number ($\mathcal{M}$) for low-angular momentum flow with $\mathcal{E}_0 = 1.001$, $\lambda_0 = 2.26$, and $\beta_0 = 10^2$, (b) for the SANE FM torus. Panels (c), (d), and (e) are showing vertically and time-averaged Mach number, specific energy, and specific angular momentum, respectively. The low angular momentum simulation is shown in black color, with the FM torus simulation in red color. We observe that both results remain very similar near the black hole; however, there are some differences in the outer disc. Furthermore, the transition from subsonic to supersonic in the flow is almost at the same radius, indicating that a low angular momentum flow with a high magnetic field is very much similar to the usual torus settings.

REFERENCES

Abramowicz, M. A., Czerny, B., Lasota, J. P., & Szuszkiewicz, E. 1988, Astrophys. J., 332, 646, doi: 10.1086/166683

Akiyama, K., et al. 2022, Astrophys. J. Lett., 930, L16, doi: 10.3847/2041-8213/ac6672

Balbus, S. A., & Hawley, J. F. 1991, Astrophys. J., 376, 214, doi: 10.1086/170270

Balbus, S. A., & Hawley, J. F. 1998, Rev. Mod. Phys., 70, 1, doi: 10.1103/RevModPhys.70.1

Belloni, T. M., Motta, S. E., & Munoz-Darias, T. 2011, Bull. Astron. Soc. India, 39, 409. https://arxiv.org/abs/1109.3388

Bhowmick, R., Debnath, D., Chatterjee, K., et al. 2021, Astrophys. J., 910, 138, doi: 10.3847/1538-4357/abe134

Blandford, R. D., & Znajek, R. L. 1977, MNRAS, 179, 433, doi: 10.1093/mnras/179.3.433

Chakrabarti, S. K. 1989, ApJ, 347, 365, doi: 10.1086/168125

Chakrabarti, S. K. 1990, Theory of Transonic Astrophysical Flows, doi: 10.1142/1091

Chakrabarti, S. K. 1996a, Phys. Rept., 266, 229, doi: 10.1016/0370-1573(95)00057-7

Chakrabarti, S. K. 1996b, Mon. Not. Roy. Astron. Soc., 283, 325, doi: 10.1093/mnras/283.1.325

Chakrabarti, S. K. 1996c, Astrophys. J., 464, 664, doi: 10.1086/177354

Chakrabarti, S. K. 2018, in Fourteenth Marcel Grossmann Meeting - MG14, ed. M. Bianchi, R. T. Jansen, & R. Ruffini, 369–384, doi: 10.1142/9789813226609_0020

Chakrabarti, S. K., Acharyya, K., & Molteni, D. 2004, A&A, 421, 1, doi: 10.1051/0004-6361:20034523

Chakrabarti, S. K., & Das, S. 2004, Mon. Not. Roy. Astron. Soc., 349, 649, doi: 10.1111/j.1365-2966.2004.07536.x

Chakrabarti, S. K., Debnath, D., & Nagarkoti, S. 2019, Adv. Space Res., 63, 3749, doi: 10.1016/j.asr.2019.02.014

Chan, H.-S., Dhang, P., Dexter, J., & Begelman, M. C. 2025, ApJ, 985, 135, doi: 10.3847/1538-4357/adce7f

Chattopadhyay, I., & Kumar, R. 2016, MNRAS, 459, 3792, doi: 10.1093/mnras/stw876

Cuadra, J., Nayakshin, S., & Martins, F. 2008, MNRAS, 383, 458, doi: 10.1111/j.1365-2966.2007.12573.x

Das, S. 2007, MNRAS, 376, 1659, doi: 10.1111/j.1365-2966.2007.11501.x

Das, S., & Chakrabarti, S. K. 2004, International Journal of Modern Physics D, 13, 1955, doi: 10.1142/S0218271804005912

Das, S., Chattopadhyay, I., & Chakrabarti, S. K. 2001, ApJ, 557, 983, doi: 10.1086/321692

Das, S., Chattopadhyay, I., Nandi, A., & Molteni, D. 2014, MNRAS, 442, 251, doi: 10.1093/mnras/stu864

Dihingia, I. K., Das, S., Maity, D., & Chakrabarti, S. 2018a, PhRvD, 98, 083004, doi: 10.1103/PhysRevD.98.083004

Dihingia, I. K., Das, S., Maity, D., & Nandi, A. 2019a, Mon. Not. Roy. Astron. Soc., 1852, doi: 10.1093/mnras/stz1933

Dihingia, I. K., Das, S., & Mandal, S. 2018b, MNRAS, 475, 2164, doi: 10.1093/mnras/stx3269

Dihingia, I. K., Das, S., & Nandi, A. 2019b, Mon. Not. Roy. Astron. Soc., 484, 3209, doi: 10.1093/mnras/stz168

Dihingia, I. K., Das, S., Prabhakar, G., & Mand al, S. 2020, MNRAS, 496, 3043, doi: 10.1093/mnras/staa1687

Dihingia, I. K., Uniyal, A., & Mizuno, Y. 2025, arXiv e-prints, arXiv:2506.05750, doi: 10.48550/arXiv.2506.05750

Dihingia, I. K., Vaidya, B., & Fendt, C. 2021, MNRAS, 505, 3596, doi: 10.1093/mnras/stab1512

Fishbone, L. G., & Moncrief, V. 1976, ApJ, 207, 962, doi: 10.1086/154565

Fryer, C. L. 1999, Astrophys. J., 522, 413, doi: 10.1086/307647

Fukue, J. 1987, PASJ, 39, 309

Garain, S. K., & Kim, J. 2023, MNRAS, 519, 4550, doi: 10.1093/mnras/stac3736

Garg, A., Rawat, D., & Méndez, M. 2024, MNRAS, 531, 585, doi: 10.1093/mnras/stae1198

Giri, K., Chakrabarti, S. K., Samanta, M. M., & Ryu, D. 2010, MNRAS, 403, 516, doi: 10.1111/j.1365-2966.2009.16147.x

Hawley, J. F., Guan, X., & Krolik, J. H. 2011, The Astrophysical Journal, 738, 84

Hawley, J. F., Richers, S. A., Guan, X., & Krolik, J. H. 2013, Astrophys. J., 772, 102, doi: 10.1088/0004-637X/772/2/102

Huang, J.-X., & Singh, C. B. 2025, Research in Astronomy and Astrophysics, 25, 025013, doi: 10.1088/1674-4527/ada2e8

Kim, J., Garain, S. K., Balsara, D. S., & Chakrabarti, S. K. 2017, MNRAS, 472, 542, doi: 10.1093/mnras/stx1986

Kim, J., Garain, S. K., Chakrabarti, S. K., & Balsara, D. S. 2019, MNRAS, 482, 3636, doi: 10.1093/mnras/sty2953

Komissarov, S. 2001, Monthly Notices of the Royal Astronomical Society, 326, L41, doi: 10.1046/j.1365-8711.2001.04863.x

Kumar, A., Chakrabarti, S., & Das, S. 2025, Astrophys. J., 980, 68, doi: 10.3847/1538-4357/adabc8

Kumar, R., & Chattopadhyay, I. 2013, MNRAS, 430, 386, doi: 10.1093/mnras/sts641

Kwan, T. M., Dai, L., & Tchekhovskoy, A. 2023, ApJL, 946, L42, doi: 10.3847/2041-8213/acc334

Lanzafame, G., Molteni, D., & Chakrabarti, S. K. 1998, MNRAS, 299, 799, doi: 10.1046/j.1365-8711.1998.01816.x

Liska, M., Tchekhovskoy, A., Ingram, A., & van der Klis, M. 2019, Mon. Not. Roy. Astron. Soc., 487, 550, doi: 10.1093/mnras/stz834

Majumder, S., Kushwaha, A., Singh, S., et al. 2025, arXiv e-prints, arXiv:2506.03774, doi: 10.48550/arXiv.2506.03774

McKinney, J. C., Tchekhovskoy, A., & Blandford, R. D. 2012, Mon. Not. Roy. Astron. Soc., 423, 3083, doi: 10.1111/j.1365-2966.2012.21074.x

Melia, F., Jokipii, J. R., & Narayanan, A. 1992, ApJL, 395, L87, doi: 10.1086/186494

Mitra, S., & Das, S. 2024, ApJ, 971, 28, doi: 10.3847/1538-4357/ad55cb

Molteni, D., Lanzafame, G., & Chakrabarti, S. K. 1994, ApJ, 425, 161, doi: 10.1086/173972

Molteni, D., Ryu, D., & Chakrabarti, S. K. 1996, Astrophys. J., 470, 460, doi: 10.1086/177877

Molteni, D., Ryu, D., & Chakrabarti, S. K. 1996a, ApJ, 470, 460, doi: 10.1086/177877

Molteni, D., Sponholz, H., & Chakrabarti, S. K. 1996b, ApJ, 457, 805, doi: 10.1086/176775

Muchotrzeb, B., & Paczynski, B. 1982, AcA, 32, 1

Murchikova, L., White, C. J., & Ressler, S. M. 2022, Astrophys. J. Lett., 932, L21, doi: 10.3847/2041-8213/ac75c3

Murchikova, L., & Witzel, G. 2021, Astrophys. J. Lett., 920, L7, doi: 10.3847/2041-8213/ac2308

Narayan, R., Igumenshchev, I. V., & Abramowicz, M. A. 2003, Publ. Astron. Soc. Jap., 55, L69, doi: 10.1093/pasj/55.6.L69

Narayan, R., & Yi, I. 1995, Astrophys. J., 452, 710, doi: 10.1086/176343

Narayan, R., Yi, I., & Mahadevan, R. 1995, Nature, 374, 623, doi: 10.1038/374623a0

Narayan, R., & Yi, I.-s. 1994, Astrophys. J. Lett., 428, L13, doi: 10.1086/187381

Novikov, I. D., & Thorne, K. S. 1973, in Les Houches Summer School of Theoretical Physics: Black Holes, 343–550

Okuda, T. 2014, MNRAS, 441, 2354, doi: 10.1093/mnras/stu738

Okuda, T., & Das, S. 2015, MNRAS, 453, 147, doi: 10.1093/mnras/stv1626

Okuda, T., & Molteni, D. 2012, MNRAS, 425, 2413, doi: 10.1111/j.1365-2966.2012.21571.x

Okuda, T., Singh, C. B., & Aktar, R. 2022, MNRAS, 514, 5074, doi: 10.1093/mnras/stac1630

Okuda, T., Singh, C. B., Das, S., et al. 2019, PASJ, 71, 49, doi: 10.1093/pasj/psz021

Olivares, H., Porth, O., Davelaar, J., et al. 2019, A&A, 629, A61, doi: 10.1051/0004-6361/201935559

Olivares, H. R., Mościbrodzka, M. A., & Porth, O. 2023, A&A, 678, A141, doi: 10.1051/0004-6361/202346010

Palit, I., Janiuk, A., & Sukova, P. 2019, MNRAS, 487, 755, doi: 10.1093/mnras/stz1296

Porth, O., Olivares, H., Mizuno, Y., et al. 2017, Computational Astrophysics and Cosmology, 4, 1, doi: 10.1186/s40668-017-0020-2

Proga, D., & Begelman, M. C. 2003, ApJ, 582, 69, doi: 10.1086/344537

Quataert, E. 2004, ApJ, 613, 322, doi: 10.1086/422973

Rees, M. J. 1988, Nature, 333, 523, doi: 10.1038/333523a0

Ressler, S. M., Quataert, E., & Stone, J. M. 2018, Mon. Not. Roy. Astron. Soc., 478, 3544, doi: 10.1093/mnras/sty1146

Ressler, S. M., Quataert, E., & Stone, J. M. 2018, MNRAS, 478, 3544, doi: 10.1093/mnras/sty1146

Rodriguez Cavero, N., Marra, L., Krawczynski, H., et al. 2023, ApJL, 958, L8, doi: 10.3847/2041-8213/acfd2c

Ryu, D., Brown, G. L., Ostriker, J. P., & Loeb, A. 1995, ApJ, 452, 364, doi: 10.1086/176308

Shakura, N. I., & Sunyaev, R. A. 1973, Astron. Astrophys., 24, 337

Singh, C. B., Okuda, T., & Aktar, R. 2021, arXiv e-prints, arXiv:2101.05474. https://arxiv.org/abs/2101.05474

Smith, D. M., Heindl, W. A., & Swank, J. H. 2002, Astrophys. J., 569, 362, doi: 10.1086/339167

Sponholz, H., & Molteni, D. 1994, Mon. Not. Roy. Astron. Soc., 271, 233, doi: 10.1093/mnras/271.1.233

Steiner, J. F., Nathan, E., Hu, K., et al. 2024, ApJL, 969, L30, doi: 10.3847/2041-8213/ad58e4

Suková, P., Charzyński, S., & Janiuk, A. 2017, MNRAS, 472, 4327, doi: 10.1093/mnras/stx2254

Tauris, T. M., & van den Heuvel, E. P. J. 2003, https://arxiv.org/abs/astro-ph/0303456

Tchekhovskoy, A., & McKinney, J. C. 2012, Mon. Not. Roy. Astron. Soc., 423, 55, doi: 10.1111/j.1745-3933.2012.01256.x

Tchekhovskoy, A., Narayan, R., & McKinney, J. C. 2010, Astrophys. J., 711, 50, doi: 10.1088/0004-637X/711/1/50

Tchekhovskoy, A., Narayan, R., & McKinney, J. C. 2011, Mon. Not. Roy. Astron. Soc., 418, L79, doi: 10.1111/j.1745-3933.2011.01147.x

Wielgus, M., et al. 2022, Astrophys. J. Lett., 930, L19, doi: 10.3847/2041-8213/ac6428

Yuan, F., & Narayan, R. 2014, Ann. Rev. Astron. Astrophys., 52, 529, doi: 10.1146/annurev-astro-082812-141003

Zanni, C., Ferrari, A., Rosner, R., Bodo, G., & Massaglia, S. 2007, A&A, 469, 811, doi: 10.1051/0004-6361:20066400